

# Symplectic time-domain finite element method (STD-FEM) for room acoustic modeling

Csaba Huszty<sup>1</sup>

ENTEL Engineering Research & Consulting Ltd., H-1025 Budapest, Szépvölgyi út 32., Hungary

Ferenc Izsák<sup>2</sup>

Department of Applied Analysis and Computational Mathematics, Eötvös Loránd University,  
H-1117 Budapest, Pázmány P. stny. 1.C, Hungary &

Alfréd Rényi Institute of Mathematics, H-1053 Budapest, Reáltanoda str. 13-15, Hungary

## ABSTRACT

*A new, extended symplectic time-domain finite element method (STD-FEM) is proposed for room acoustic modeling. As a mathematical model for sound propagation and reflection, the classical time-domain wave equations are used, which can be extended with air absorption. Frequency-dependent locally reactive boundary conditions are also introduced to the model. Spatially, a third-order tensor product type spectral element discretization is applied, which allows us to use explicit time steps. For this purpose, a partitioned Runge–Kutta method is employed, which is an extension of a third-order symplectic time-discretization. The method is validated on a number of examples and the performance and stability benefits are presented. We present the implementation of the method in the soundy.ai application.*

## 1. INTRODUCTION

Simulation of wave propagation for room acoustic applications is a fundamental tool in engineering analysis. Having the approximation of the full wave field at hand, many practical acoustic parameters can be predicted, such as the reverberation time, speech clarity or sound strength. For this, as a governing equation, the well-known wave equation is used assuming a lossless homogeneous medium. At the same time, these computations involve a real challenge even for relatively small rooms and even when assuming locally reacting boundaries. Challenges include setting up a realistic room and boundary model, where the frequency-dependent boundary properties of the walls are taken into account, or to set up a computationally affordable yet acceptably accurate framework. Although the spatial differential operator can easily be discretized using several approaches, all of these have their own limitations. As a common limitation, we have to choose a sufficiently fine spatial grid (or in general, a wide function space) to simulate a wide range of frequencies. Also, the corresponding time-step should satisfy a strict upper bound (the so-called CFL condition) leading to numerically stable simulations. This can also be recognized as a necessity of a high sampling frequency. This, together with the large number of spatial parameters can result in excessive computational costs even if the boundary surfaces are only locally reactive.

A number of additional specific challenges also arise.

- Material parameters for extended reactivity are not available. Even locally reactive frequency-dependent impedances are widely unavailable. In lack of these, boundary conditions need to be estimated [1].
- An accurate model, particularly at higher frequencies in large rooms, should also take into account the absorption of air. For this, both formulating the governing equations and

---

<sup>1</sup>huszty.csaba@entel.hu

<sup>2</sup>ferenc.izsak@ttk.elte.hu

implementing efficient numerical simulations are still up-to-date problems with a number of approaches [2], [3].

- From a practical point of view, realistic models should include the possibility of simulating directional sound sources and the generated field sometimes has to be evaluated assuming directional receivers, particularly for spatial room acoustic parameters.
- Given the computational load and available infrastructure, the method should be scalable to some extent between CPU and RAM usage.
- In real-life situations, the computational domain has a complex geometry. The furniture or any existing equipment makes the spatial discretization even for a conventional rectangular room highly non-trivial.

In the framework of the present paper, we present only a portion of the above issues with further solutions presented in future works. Our current focus is to increase the efficiency of the simulations in two ways.

First, we aim at reducing the sampling frequency in the simulations as far as possible to reduce the computational load. For this, we will extend a recent symplectic partitioned Runge–Kutta method, which was introduced for the simulation of seismic waves in [4] and analyzed further in [5]. To achieve this goal, we also need an efficient finite element discretization of the spatial differential operator. We made use the conventional spectral element space, which was introduced in [6] and developed in a number of ways [7]. An important merit of our approach is that we may apply fully explicit and relatively large time steps effectively reducing the computational time.

Second, we implement frequency-dependent impedances so that the boundary conditions are embedded into the corresponding variational form, and the corresponding discretization will be expressed as a matrix-vector form. The prototype of the computational algorithm is implemented in Matlab. Here, we have to make use sparse matrix operations and minimize the number of matrix-vector products.

Finally, a number of simulation results are presented together with an experimental analysis of their performance.

### 1.1. Related work

The application of spectral finite elements was proposed in computational geosciences [6]. The methodology was adapted for simulations in acoustics [8] pointing out the advances of this approach. Incorporating the real life situation with frequency-dependent boundary conditions, conventional finite elements were also applied in [9]. This framework contains locally reacting surfaces. Parallel with this, a spectral finite element based approach was developed in [10]. A highly flexible space-discretization is offered by the family of discontinuous Galerkin methods. In this framework, the local polynomial basis can be chosen element-by-element allowing local spatial refinement in a fixed grid [11]. Concerning the time stepping, a fourth-order implicit-explicit Runge–Kutta time stepping method was used in [10], while explicit Runge–Kutta methods of different orders in [9]. At the same time, until now, for room acoustics purposes, symplectic Runge–Kutta time discretizations were not applied.

## 2. MATERIALS AND METHODS

For the simulation of the acoustic waves in a room given with  $\Omega \subset \mathbb{R}^3$  over the time interval  $(0, T)$ , we use the wave equation

$$\begin{cases} \partial_{tt}p(t, \mathbf{x}) = c^2 \Delta p(t, \mathbf{x}) & (t, \mathbf{x}) \in (0, T) \times \Omega \\ p(0, \mathbf{x}) = p_0(\mathbf{x}) & \mathbf{x} \in \Omega \\ \partial_t p(0, \mathbf{x}) = p_{t,0}(\mathbf{x}) & \mathbf{x} \in \Omega \end{cases} \quad (1)$$

for the unknown pressure  $p$ . This will be later equipped with some realistic frequency-dependent boundary conditions. Here  $c$  is the speed of sound and the initial functions  $p_0$  and  $p_{t,0}$  are given. In the simulation part, SI units are used so we do not display units.

For incorporating the boundary conditions, we recall that the impedance - as a space-dependent function  $Z : \partial\Omega \rightarrow \mathbb{R}$  - can be given as

$$Z(\mathbf{x}) = \frac{p(\mathbf{x})}{\boldsymbol{\nu} \cdot \mathbf{v}(\mathbf{x})} \quad \mathbf{x} \in \partial\Omega, \quad (2)$$

where  $\mathbf{v} : \Omega \rightarrow \mathbb{R}^3$  is the virtual particle speed in the model and  $\boldsymbol{\nu} : \partial\Omega \rightarrow \mathbb{R}^3$  denotes the outward normal, which is defined almost everywhere. Using the identity

$$\nabla p(t, \mathbf{x}) = -\rho_0 \cdot \partial_t \mathbf{v}(t, \mathbf{x}) \quad \mathbf{x} \in \Omega,$$

with the density  $\rho_0 = 1.205$  of the air together with Equation 2, we obtain the equality

$$\partial_{\boldsymbol{\nu}} p(t, \mathbf{x}) = \boldsymbol{\nu} \cdot \nabla p(t, \mathbf{x}) = -\rho_0 \partial_t \boldsymbol{\nu} \cdot \mathbf{v}(t, \mathbf{x}) = -\frac{\rho_0}{Z} \cdot \partial_t p(t, \mathbf{x}) \quad \mathbf{x} \in \partial\Omega. \quad (3)$$

Extending Equation 2, in the framework of a frequency-dependent model, the response of the surface is given by the equality

$$\boldsymbol{\nu} \cdot \mathbf{v}(t, \mathbf{x}) = a_0(\mathbf{x}) \cdot p(t, \mathbf{x}) + a_1(\mathbf{x}) \cdot p(t - \tau, \mathbf{x}) + \dots + a_N(\mathbf{x}) \cdot p(t - N\tau, \mathbf{x}). \quad (4)$$

Indeed, depending on the frequency, the impedance will contain also a delay term. In this way, a wave containing arbitrary frequencies can be decomposed by the sum on the right hand side of Equation 4. Also, the coefficients  $a_0, a_1, \dots, a_N$  depend also on the delay term  $\tau$ . These will be computed with a subroutine, using the inputs:  $N, \tau$  and the kind of the material on the boundary.

## 2.1. Variational form and discretization

Using Equation 3, our boundary condition in Equation 4 can be recognized as a Neumann-type boundary condition and can be used to derive a variational form of the original wave problem in Equation 1 as follows:

$$\partial_{\boldsymbol{\nu}} p(t, \mathbf{x}) = -\rho_0 \partial_t \boldsymbol{\nu} \cdot \mathbf{v}(t, \mathbf{x}) = -\rho_0 \cdot (a_0 \cdot \partial_t p(t, \mathbf{x}) + a_1 \cdot \partial_t p(t - \tau, \mathbf{x}) + \dots + a_N \cdot \partial_t p(t - N\tau, \mathbf{x})). \quad (5)$$

For the spatial discretization, we use the approximation

$$p(t, \mathbf{x}) \approx p_h(t, \mathbf{x}) = \sum_j p_j(t) b_j(\mathbf{x}) \quad (6)$$

with a given finite element basis  $\{b_j\}_{j \in J}$ . Accordingly, in each  $t$ , we have to approximate the components of the vector function  $\mathbf{u}(t) = [u_1(t), u_2(t), \dots]^T$ .

Using these, for any basis function  $b_k$ , we have

$$\begin{aligned} \int_{\Omega} \Delta p(t, \mathbf{x}) b_k(\mathbf{x}) \, d\mathbf{x} &\approx \int_{\Omega} \sum_{j \in J} p_j(t) \cdot \Delta b_j(\mathbf{x}) b_k(\mathbf{x}) \, d\mathbf{x} \\ &= - \sum_{j \in J} p_j(t) \int_{\Omega} \nabla b_j(\mathbf{x}) \cdot \nabla b_k(\mathbf{x}) \, d\mathbf{x} + \sum_{j \in J_b} p_j(t) \int_{\partial\Omega} \partial_{\boldsymbol{\nu}} b_j(\mathbf{x}) b_k(\mathbf{x}) \, d\mathbf{x}. \end{aligned} \quad (7)$$

For the matrix-vector form, we use the matrices  $S, W \in \mathbb{R}^{|J| \times |J|}$  given by  $S[j, k] = \int_{\Omega} \nabla b_j \cdot \nabla b_k$  and  $W[j, k] = \int_{\Omega} b_j b_k$ , respectively. We also need the matrix  $W_b \in \mathbb{R}^{|J_b| \times |J|}$  with  $W_b[j, k] = \int_{\partial\Omega} b_j b_k$ .

Introducing the matrices

$$L = -c^2 \cdot W^{-1}S \quad \text{and} \quad M = -c^2 \cdot \rho_0 \cdot a_0 W^{-1}QW_b, \quad (8)$$

with the auxiliary function  $\mathbf{w} = \partial_t \mathbf{p}$  and taking all possible basis functions  $b_k$  in Equation 7, we obtain the linear system

$$\partial_t \begin{pmatrix} \mathbf{p}(t) \\ \mathbf{w}(t) \end{pmatrix} = \begin{pmatrix} \mathbf{w}(t) \\ L\mathbf{p}(t) + M\tilde{\mathbf{w}}(t) \end{pmatrix}, \quad (9)$$

where the discrete delay term

$$\tilde{\mathbf{w}}(t) = \mathbf{a}_0 * \mathbf{w}(t) + \mathbf{a}_1 * \mathbf{w}(t - \tau) + \mathbf{a}_2 * \mathbf{w}(t - 2\tau) \cdots + \mathbf{a}_N * \mathbf{w}(t - N\tau)$$

was applied. For the time discretization, we also need its iterated version

$$\tilde{\tilde{\mathbf{w}}}(t) = \mathbf{a}_0 * \tilde{\mathbf{w}}(t) + \mathbf{a}_1 * \tilde{\mathbf{w}}(t - \tau) + \mathbf{a}_2 * \tilde{\mathbf{w}}(t - 2\tau) \cdots + \mathbf{a}_N * \tilde{\mathbf{w}}(t - N\tau)$$

and the following quantity

$$\tilde{\mathbf{p}}(t) = \mathbf{a}_0 * \mathbf{p}(t) + \mathbf{a}_1 * \mathbf{p}(t - \tau) + \mathbf{a}_2 * \mathbf{p}(t - 2\tau) \cdots + \mathbf{a}_N * \mathbf{p}(t - N\tau),$$

where the operation  $*$  yields pointwise multiplication. In the same fashion, we can define the terms  $\tilde{\tilde{\mathbf{w}}}$  and  $\tilde{\tilde{L\mathbf{p}}}$ , which are also needed in the final scheme.

The above spatial discretization was performed using a tensor product type third-order and fourth-order spectral finite element space  $V_h = \text{span} \{b_j\}_{j \in J}$ . For this, we applied a rectangular grid in a brick-shaped domain  $\Omega$ , which is called the coarse grid. In each brick, besides the vertices, in the spatially third-order case, we have altogether  $4 \cdot 4 \cdot 4$  grid points: 2 in the interior of edges,  $2 \cdot 2$  in the interior of faces and  $2 \cdot 2 \cdot 2$  in the interior of the brick. Accordingly, in the spatially fourth-order case, these numbers are increased by one.

For the time discretization, we use an extended symplectic partitioned Runge–Kutta method [12]. In concrete terms, concerning the numerical solution of the simple wave equation

$$\partial_t \begin{pmatrix} \mathbf{p}(t) \\ \mathbf{w}(t) \end{pmatrix} = \begin{pmatrix} \mathbf{w}(t) \\ L\mathbf{p}(t) + M\tilde{\mathbf{w}}(t) \end{pmatrix} \quad (10)$$

a new third-order symplectic scheme was derived in [4] for simulating seismic waves. This was analyzed further in [5]. We made a step forward by incorporating extra terms such that

- it applies to the linear system in Equation 9,
- it still delivers a third-order accuracy in time.

## 2.2. Computational scheme and implementation details

According to the above requirements, we use the following time stepping.

- (f-i) We start from the vectors  $\mathbf{p}^n$  and  $\mathbf{w}^n$ ,
- (f-ii)  $\mathbf{p}_1^n = \mathbf{p}^n + \delta t \cdot \frac{1}{4} \mathbf{w}^n$ ,
- (f-iii)  $\mathbf{w}_1^n = \mathbf{w}^n + \delta t \cdot \frac{2}{3} (L\mathbf{p}_1^n + M\tilde{\mathbf{w}}^n)$ ,
- (f-iv)  $\mathbf{p}^{n+1} = \mathbf{p}_1^n + \delta t \cdot \frac{3}{4} \mathbf{w}_1^n + (\delta t)^3 \cdot \frac{1}{24} (L\mathbf{w}_1^n + 4M(\tilde{L\mathbf{p}}_1^n + M\tilde{\tilde{\mathbf{w}}}^n))$ ,
- (f-v)  $\mathbf{w}^{n+1} = \mathbf{w}_1^n + \delta t \cdot (\frac{1}{3} \cdot L\mathbf{p}^{n+1} + \frac{1}{3} \cdot M\tilde{\mathbf{w}}_1^n) + (\delta t)^2 \cdot \frac{5}{18} M(\tilde{L\mathbf{p}}_1^n + M\tilde{\tilde{\mathbf{w}}}^n) + (\delta t)^3 \cdot (\frac{1}{6} \cdot M^2(\tilde{\tilde{L\mathbf{p}}}_1^n + M\tilde{\tilde{\tilde{\mathbf{w}}}}}^n) + \frac{1}{24} \cdot ML\tilde{\mathbf{w}}^n)$ .

We omit here the lengthy derivation of the above scheme, instead, we state two important properties of it. Firstly, the scheme in (f-i) – (f-v) is a partitioned Runge–Kutta method of third order accuracy (in time). Secondly, omitting the boundary terms, the scheme in (f-i) – (f-v) is symplectic. Our computer program consists of two parts:

- First, in the initialization stage, we perform the space discretization building up the matrices  $M$  and  $L$  together with the initial conditions. Then we estimate the largest admissible time step preserving stability. Also, the length  $N$  of the delay term is determined and the corresponding coefficients  $\mathbf{a}_0, \mathbf{a}_1, \dots, \mathbf{a}_N$  is computed using a subroutine. For the details, we refer to [13].
- In the second, the time stepping stage, over a number of time steps given in (f-i)–(f-v), we compute the pressure on the entire domain  $\Omega$ . Practically, only the pressure is used to test and evaluate our method.

### 3. SIMULATION RESULTS

In each of the consecutive one and three-dimensional numerical experiments, as an initial condition, we took a Gaussian pulse

$$\begin{pmatrix} p(0, \mathbf{x}) \\ w(0, \mathbf{x}) \end{pmatrix} = \begin{pmatrix} e^{-\frac{r^2}{d^2}} \\ -\frac{c}{2r}e^{-\frac{r^2}{d^2}} + \frac{1}{2} \cdot e^{-\frac{r^2}{d^2}} \cdot \frac{2rc}{d^2} + \frac{c}{2r}e^{-\frac{r^2}{d^2}} + \frac{1}{2} \cdot e^{-\frac{r^2}{d^2}} \cdot \frac{-2rc}{d^2} \end{pmatrix} = \begin{pmatrix} e^{-\frac{r^2}{d^2}} \\ 0 \end{pmatrix}. \quad (11)$$

Here  $r = |\mathbf{x} - \mathbf{x}_0|$ , with a fixed  $\mathbf{x}_0 \in \Omega$ , where the pulse is starting from and  $d$  is a free parameter. Since both  $p$  and  $w$  can be considered as zero on the boundary  $\partial\Omega$  (also over a few first time steps), the boundary terms including the delay terms will be initiated as zero.

**One-dimensional case** Now, omitting the boldface notations, the analytic solution of the equation

$$\begin{cases} \partial_{tt}p(t, x) = c^2 \partial_{xx}p(t, x) & t \in (0, T), x \in \mathbb{R}^+ \\ p(0, x) = e^{-\frac{(x-x_0)^2}{d^2}} & x \in \mathbb{R}^+ \\ \partial_t p(0, x) = 0 & x \in \mathbb{R}^+ \\ -\partial_\nu p(t, 0) = \partial_x p(t, 0) = \rho_0 a_0 \cdot \partial_t p(t, 0) = \frac{\rho_0}{Z} \cdot \partial_t p(t, 0) & t \in (0, T), \end{cases} \quad (12)$$

can be given as

$$p(t, x) = \frac{1}{2}e^{-\frac{(x-x_0-ct)^2}{d^2}} + S_r \cdot \frac{1}{2}H(ct - x) \cdot e^{-\frac{(-x-x_0-ct)^2}{d^2}} + \frac{1}{2}e^{-\frac{(x-x_0+ct)^2}{d^2}} + S_l \cdot \frac{1}{2}H(ct - x) \cdot e^{-\frac{(-x-x_0+ct)^2}{d^2}}, \quad (13)$$

where  $H$  denotes the Heaviside function, and the coefficients are given with

$$S_r = \frac{2}{2\sqrt{1-\alpha}} = \frac{1}{\sqrt{1-\alpha}} \quad \text{and} \quad S_l = \sqrt{1-\alpha}.$$

This is a model of wave propagation on the positive half axis with an impedance boundary condition on the wall at zero. Whenever it does not contain a distributed delay, here we can test the numerical treatment of the boundary condition in Equation 3.

**Three-dimensional case** To compare our simulation results with the propagation of the direct sound, we also note that using polar coordinates, the initial conditions in Equation 11 imply

$$p(t, r) = \frac{r-ct}{2r}e^{-\frac{(r-ct)^2}{d^2}} + \frac{r+ct}{2r}e^{-\frac{(r+ct)^2}{d^2}} \quad (14)$$

as the solution of Equation 1 for  $\Omega = \mathbb{R}^3$ .

In the following series of experiments, we simulate a single reflection of the initial Gaussian pulse. To validate this, we have derived a semi-analytic solution simulating the reflection of the pressure wave from the ceiling in a rectangular room  $\Omega = (0, L_x) \times (0, L_y) \times (0, L_z)$ . In concrete terms, we approximate the solution of

$$\begin{cases} \partial_{tt}p(t, \mathbf{x}) = c^2 \Delta p(t, \mathbf{x}) & t \in (0, T), \mathbf{x} \in \Omega \\ p(0, \mathbf{x}) = e^{-\frac{(\mathbf{x}-\mathbf{x}_0)^2}{d^2}} & \mathbf{x} \in \Omega \\ \partial_t p(0, \mathbf{x}) = 0 & \mathbf{x} \in \Omega \\ -\partial_z p(t, \mathbf{x}^+) = \frac{\rho_0}{Z(\mathbf{x}^+)} \cdot \partial_t p(t, \mathbf{x}^+) & t \in (0, T), \mathbf{x}^+ \in (0, L_x) \times (0, L_y) \times L_z \\ -\partial_\nu p(t, \mathbf{x}^+) = \frac{\rho_0}{Z(\mathbf{x}^+)} \cdot \partial_t p(t, \mathbf{x}^+) & t \in (0, T), \mathbf{x}^+ \in \partial\Omega \setminus (0, L_x) \times (0, L_y) \times L_z, \end{cases} \quad (15)$$

where in the last two lines, the boundary condition is given separately on the ceiling and the remaining part of the boundary. Using the notation for  $\bar{\mathbf{x}}_0$  the mirror image of  $\mathbf{x}_0$  with respect to the ceiling, the semi-analytic solution has the form

$$p(t, \mathbf{x}) = \frac{r - ct}{2r} e^{-\frac{(r-ct)^2}{d^2}} + S_R \cdot \frac{r^* - ct}{2r^*} H(ct - r_0) \cdot e^{-\frac{(-r^*-ct)^2}{d^2}}, \quad (16)$$

where  $r = |\mathbf{x} - \mathbf{x}_0|$ ,  $r^* = |\mathbf{x} - \bar{\mathbf{x}}_0|$  and  $r^* = \frac{1}{2} \cdot |\mathbf{x}_0 - \bar{\mathbf{x}}_0|$ . The coefficient  $S_R$  can be computed using the boundary condition in the fourth line of Equation 15.

The “solution” in Equation 16 is semi-analytic, since in the derivations, the coefficient  $S_R$  was assumed to be time-independent, only the reflection from the ceiling is taken into account, the effect of the second (back-propagating) term in Equation 14 is omitted.

In the second series of experiments, we have implemented the boundary conditions in Equation 5, which can be inserted instead of the second two lines in Equation 15. In this case, we have no analytic (or semi-analytic) reference available.

### 3.1. Experimental analysis

First, a series of one-dimensional simulations were performed. Since the analytic solution is known (see Equation 13), we can investigate the relation of spatial and time parameters regarding the error and the stability.

#### 1.1 One-dimensional experiments

We have performed a series of numerical experiments with different coarse spatial grid spacing  $h$  between 0.05 and 0.13 and different time steps  $\delta t$  between 0.00002 and 0.00007. In each case, we have computed the relative discrete  $L_2$ -error, which is defined with

$$\frac{\sqrt{\sum_{x_k \in \text{grid}} (p(T, x_k) - p_k^T)^2}}{\sqrt{\sum_{x_k \in \text{grid}} (p(T, x_k))^2}} \quad (17)$$

of the pressure term, where  $h$  denotes the (uniform) grid spacing and  $p_k^T$  the approximation at the final time  $T$  in the  $k$ -th grid point. We applied fourth-order spectral finite elements combined with the third-order time stepping in (f-i)-(f-v).

The corresponding results are shown in Figure 1.

In each case, we have initiated a Gaussian initial condition (see Equation 11) with  $d = 0.08$  and

performed the simulation until  $T = 0.075$  s using the impedance parameter  $\alpha = 0.4$  on the left-hand wall. Note that the simulation delivers a reliable result until the frequency limit  $\approx 1700$  Hz. Whenever this is only a particular case, the Gaussian pulse with  $d_* = k \cdot 0.08$  can be represented in the same way on the spatial grid  $h_* = k \cdot h$  and we can use the time step  $\delta t_* = k \cdot \delta t$  in the simulations. Accordingly, this gives a reliable result until the frequency limit  $\approx \frac{1}{k} \cdot 1700$  Hz.

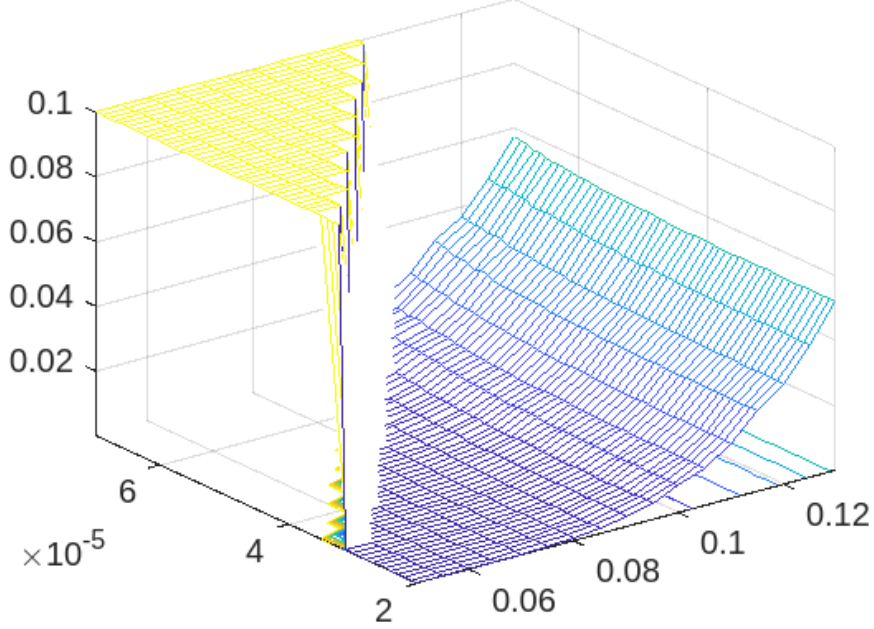


Figure 1: Relative error (see Equation 17) of reflected sound for various coarse grid spacings ( $x$  axis) and time-steps ( $y$  axis) starting from the initial pulse  $e^{-\frac{(x-4)^2}{0.08^2}}$ . The final time is 0.075 s. The yellow region exhibits the minimum of 0.1 and the relative error, yielding instability.

One can observe that in this regime, decreasing the time step, the computational error is only slightly decreased. In other words, we should apply the largest possible time step until the scheme remains stable.

**Stability limits** To optimize the computational costs, we should relax unnecessary restrictions regarding the time steps. This is usually measured with the so-called CFL number, which emerges in the stability condition

$$\delta t \lesssim \text{CFL} \cdot \frac{h_{\min}}{c},$$

where  $h_{\min}$  denotes the minimal grid length taking into account all dimensions, see [10]. Indeed, we have to take the minimal constant for pairs  $(\delta t, h)$  ensuring stability. The range  $\text{CFL} \approx 1$  yields good stability properties and implies a physically reasonable restriction to  $\delta t$ . We also note that a uniform coarse grid  $h$  for 4-th order finite element discretization results in  $h_{\min} = \frac{1-\sqrt{3}}{2} \cdot h$ . Regarding the results in Figure 1, we display its value for some parameter pairs.

The values in Table 1 indicate rather strong stability properties and a significant improvement compared to the results in [10].

## 1.2 3-dimensional experiments

Here, we have validated the implementation of the impedance type boundary condition in Equation 15 by comparing the simulation results and the semi-analytic solution in Equation 16. Also, we investigated the effect of the different spatial and time discretizations. Focusing to a single

Table 1: Experimental CFL numbers for the cases shown in Figure 1.

$\delta t$	$7 \cdot 10^{-5}$	$6.5 \cdot 10^{-5}$	$6.1 \cdot 10^{-5}$	$5.8 \cdot 10^{-5}$	$5.3 \cdot 10^{-5}$	$4.7 \cdot 10^{-5}$	$4.4 \cdot 10^{-5}$
$h$	0.095	0.09	0.085	0.08	0.075	0.07	0.065
CFL number	1.45	1.42	1.39	1.428	1.39	1.32	1.33

reflection, we applied relatively small Gaussian parameters and the receiver was placed in the vicinity of the ceiling of the room. The setup and the results of the computation are shown in Table 2 and Figure 2, respectively.

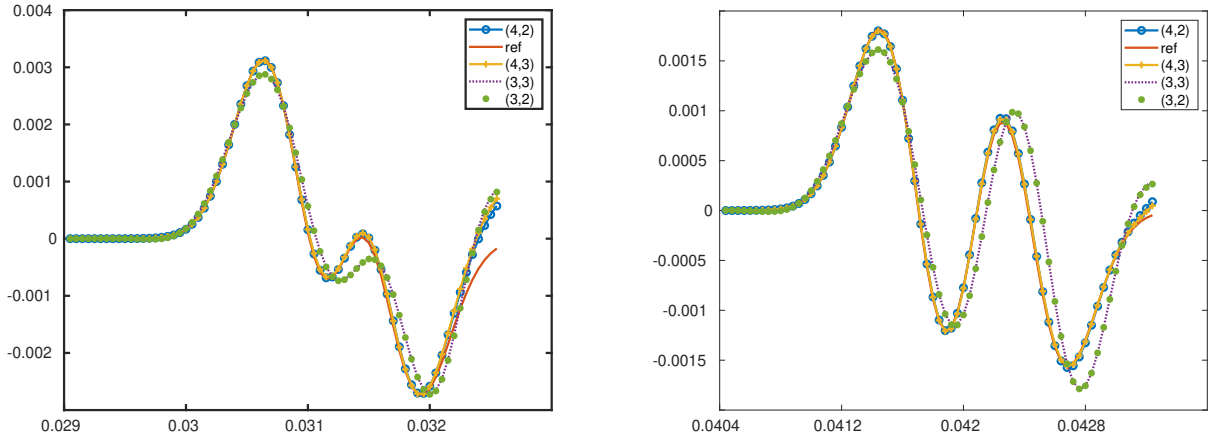


Figure 2: Pressure in the receiver  $x$  for different space and time discretization orders. Semi-analytic solution is depicted with red color. Left: Experiment 1, right: Experiment 2.

Here, the fourth-order space discretization delivers a precise approximation for both time steppings. At the same time, the third-order one exhibits better stability properties such that we can reduce the number of time steps.

Finally, in **Experiment 3**, we have implemented the boundary conditions in Equation 4. Here, we had to use all delay terms in the scheme (f-i)–(f-v). We have used the same geometry as in **Experiment 1** together with the following boundaries:

- Material of the side walls: painted concrete block.
- Material on the ceiling: painted smooth concrete.
- Material on the floor: wood parquet on concrete.
- Length of the delay term: 16.

The performance of the computations in all of the experiments is summarized in Table 3.

Since we overall compute with sparse matrices, the computational costs (including speed and memory usage) are proportional to the number of nonzero elements in the matrix  $L$ , which is displayed in the first column. For rectangular domains, the construction of the auxiliary matrices is rather quick. This is shown in the second column. The bottleneck of these simulations is the large number of time steps. The elapsed time for this phase is given in the third column.

Table 2: Parameters in the simulations of impedance type boundary conditions.

	<b>Experiment 1</b>	<b>Experiment 2</b>
Size of the computational domain $\Omega$	$15 \times 5.1 \times 3$	$19.2 \times 5.4 \times 3.6$
Volume of $\Omega$	$229.5 \text{ m}^3$	$315 \text{ m}^3$
Location of the source $\mathbf{x}_0$	(3, 3, 1.8)	(3, 3, 2.04)
Location of the receiver $\mathbf{x}$	(13.5, 3, 1.95)	(17.16, 3, 2.4)
Coarse grid size (uniform)	0.15	0.12
Sampling frequency	$2 \cdot 10^4$	$2.5 \cdot 10^4$
Number of time steps	650	1100
Length of impulse response	0.0325 s	0.044 s

Table 3: Computational costs in the simulations on a computer with i7 1185G7, 3 GHz processor.

	# of nonzeros in $L$	Time: 1st phase	2nd phase	Frequency limit
<b>Experiment 1</b> , (4,3)	70705777	1.8 s	436.3 s	907 Hz
<b>Experiment 1</b> , (4,2)	70705777	1.9 s	404.2 s	907 Hz
<b>Experiment 1</b> , (3,3)	24362791	0.64 s	136.3 s	907 Hz
<b>Experiment 1</b> , (3,2)	24362791	0.62 s	118.7 s	907 Hz
<b>Experiment 2</b> , (4,3)	223539241	5.36 s	2226.4 s	1133 Hz
<b>Experiment 2</b> , (4,2)	223539241	5.37 s	1534.2 s	1133 Hz
<b>Experiment 2</b> , (3,3)	76900876	2.03 s	930 s	1133 Hz
<b>Experiment 2</b> , (3,2)	76900876	2.02 s	844.6 s	1133 Hz
<b>Experiment 3</b> , (4,3)	70705777	2.05 s	608 s	907 Hz

#### 4. EXTENSION TO INCORPORATE AIR ABSORPTION

Extending Equation 1, as a model of sound propagation in lossy media we use the equation

$$\begin{cases} \partial_{tt} p(t, \mathbf{x}) = c^2 \Delta p(t, \mathbf{x}) + \tau \cdot c^2 \partial_t \Delta p(t, \mathbf{x}) & (t, \mathbf{x}) \in (0, T) \times \Omega \\ p(0, \mathbf{x}) = p_0(\mathbf{x}) & \mathbf{x} \in \Omega \\ \partial_t p(0, \mathbf{x}) = p_{t,0}(\mathbf{x}) & \mathbf{x} \in \Omega \end{cases} \quad (18)$$

with the sound pressure  $p$  as an unknown function. This will be again equipped with boundary conditions given in Equation 4. To rewrite Equation 18 in a variational form, we have to complete the derivation in Equation 7 by extending it with the term

$$\int_{\Omega} \partial_t (\Delta p(t, \mathbf{x})) v(\mathbf{x}) \, d\mathbf{x} = - \int_{\Omega} \nabla \partial_t p(t, \mathbf{x}) \cdot \nabla v(\mathbf{x}) \, d\mathbf{x} + \int_{\partial\Omega} \boldsymbol{\nu} \cdot \nabla \partial_t p(t, \mathbf{x}) v(\mathbf{x}) \, d\mathbf{x}. \quad (19)$$

This should be discretized for a matrix-vector form. Using again the matrices  $L$  and  $M$  in Equation 8, the scheme in Equation 9 can be completed to have

$$\partial_t \begin{pmatrix} \mathbf{p}(t) \\ \mathbf{w}(t) \end{pmatrix} = \begin{pmatrix} \mathbf{w}(t) \\ L\mathbf{p}(t) + M\tilde{\mathbf{w}}(t) \end{pmatrix} + \begin{pmatrix} \mathbf{0} \\ \tau \cdot L\mathbf{w}(t) + \tau \cdot M\widetilde{\partial_t \mathbf{w}(t)} \end{pmatrix}.$$

Making this explicit with respect to  $\partial_t \mathbf{w}(t)$  results in

$$\partial_t \begin{pmatrix} \mathbf{p}(t) \\ (I - \tau M * \mathbf{a}_0) \mathbf{w}(t) \end{pmatrix} = \begin{pmatrix} \mathbf{w}(t) \\ L \mathbf{p}(t) + M \tilde{\mathbf{w}}(t) \end{pmatrix} + \begin{pmatrix} \mathbf{0} \\ \tau \cdot L \mathbf{w}(t) + \tau \cdot M \widehat{\partial_t \mathbf{w}(t)} \end{pmatrix},$$

where we have used the notation

$$\widehat{\partial_t \mathbf{w}(t)} = \partial_t (\mathbf{a}_1 * \mathbf{w}(t - \tau) + \mathbf{a}_2 * \mathbf{w}(t - 2\tau) + \dots + \mathbf{a}_N * \mathbf{w}(t - N\tau)).$$

Using also the diagonal matrix  $M_0 = (I - \tau \cdot M_{jj} \mathbf{a}_0)^{-1}$ , we finally get

$$\partial_t \begin{pmatrix} \mathbf{p}(t) \\ \mathbf{w}(t) \end{pmatrix} = \begin{pmatrix} \mathbf{w}(t) \\ M_0(L \mathbf{p}(t) + M \tilde{\mathbf{w}}(t)) \end{pmatrix} + \begin{pmatrix} \mathbf{0} \\ M_0(\tau \cdot L \mathbf{w}(t) + \tau \cdot M \widehat{\partial_t \mathbf{w}(t)}) \end{pmatrix}. \quad (20)$$

Based on this, and using the notation  $S_0(\mathbf{p}(t), \mathbf{w}(t)) = M_0(L \mathbf{p}(t) + M \tilde{\mathbf{w}}(t) + \tau \cdot L \mathbf{w}(t) + \tau \cdot M \widehat{\partial_t \mathbf{w}(t)})$ , we can construct the following scheme, which is second order accurate in time:

- (d-i) Starting from  $[\mathbf{p}^n, \mathbf{w}^n]$ .
- (d-ii)  $\mathbf{p}_1^n = \mathbf{p}^n + \delta t \cdot \frac{1}{4} \mathbf{w}^n$
- (d-iii)  $\mathbf{w}_1^n = \mathbf{w}^n + \delta t \cdot \frac{2}{3} S_0(\mathbf{p}_1^n, \mathbf{w}^n)$
- (d-iv)  $\mathbf{p}^{n+1} = \mathbf{p}_1^n + \delta t \cdot \frac{3}{4} \mathbf{w}_1^n + (\delta t)^3 \cdot \frac{1}{24} (M_0 L \mathbf{w}_1^n)$
- (d-v)  $\mathbf{w}^{n+1} = \mathbf{w}_1^n + \delta t \cdot \frac{1}{3} S_0(\mathbf{p}^{n+1}, \mathbf{w}^n) + \frac{(\delta t)^2}{2} \left( \frac{M}{\delta t} (\tilde{\mathbf{w}}^n - \tilde{\mathbf{w}}^{n-1}) + \tau L S_0(\mathbf{p}^{n+1}, \mathbf{w}^n) + \frac{\tau M}{\delta t} (\widehat{\partial_t \mathbf{w}}^n - \widehat{\partial_t \mathbf{w}}^{n-1}) \right)$

## 5. CONCLUSIONS

We presented a new time-domain FEM framework for room acoustic simulations with the following benefits.

- The discretization scheme is flexible such that even a rectangular grid can be non-uniform, e.g., finer in the vicinity of reflecting walls.
- Using finite elements, we do not only have point-values in the approximation, but the output is inherently a continuous function and the sound pressure time series can be extracted from any physical position.
- The choice of spectral finite elements makes explicit time steps possible.
- The framework incorporated Neumann-type boundary condition as FIR filters.
- The use of symplectic time discretization results in energy preservation if the underlying physical system is also Hamiltonian (e.g., in case of free propagation or full reflection).
- The optimal stability properties of symplectic methods is still valid for the present extension. Accordingly, we can apply possibly larger time steps (or lower sampling frequency) for a given simulation bandwidth still preserving stability.

The presented computational framework can be extended to support arbitrary meshes, directional sources and receivers, and extended reactive boundary conditions which will be presented in a future work.

## ACKNOWLEDGEMENTS

This work was supported by ENTEL Engineering Research & Consulting Ltd. F. Izsák acknowledges the support of the National Research, Development and Innovation Office within the framework of the Thematic Excellence Program 2021 - National Research Sub programme: “Artificial intelligence, large networks, data security: mathematical foundation and applications”.

## REFERENCES

1. A.G. Prinn, A. Walther, and E.A.P. Habets. Estimation of locally reacting surface impedance at modal frequencies using an eigenvalue approximation technique. *The Journal of the Acoustical Society of America*, 150(4):2921–2935, 2021.
2. J. M. Kates and E.J. Brandewie. Adding air absorption to simulated room acoustic models. *The Journal of the Acoustical Society of America*, 148(5):EL408–EL413, 2020.
3. B. Hamilton and S. Bilbao. Time-domain modeling of wave-based room acoustics including viscothermal and relaxation effects in air. *JASA Express Letters*, 1(9), 09 2021. 092401.
4. S. Liu, D. Yang, and J. Ma. A modified symplectic PRK scheme for seismic wave modeling. *Computers & Geosciences*, 99:28–36, 2017.
5. S. Liu, D. Yang, C. Lang, W. Wang, and Z. Pan. Modified symplectic schemes with nearly-analytic discrete operators for acoustic wave simulations. *Computer Physics Communications*, 213:52–63, 2017.
6. D. Komatitsch and J-P. Vilotte. The spectral element method: An efficient tool to simulate the seismic response of 2d and 3d geological structures. *Bulletin of the Seismological Society of America*, 88(2):368 – 392, 1998.
7. S. Geevers, W. A. Mulder, and J. J. W. van der Vegt. Efficient quadrature rules for computing the stiffness matrices of mass-lumped tetrahedral elements for linear wave problems. *SIAM J. Sci. Comput.*, 41(2):A1041–A1065, 2019.
8. G. Seriani. A parallel spectral element method for acoustic wave modeling. *Journal of Computational Acoustics*, 05(01):53–69, 1997.
9. T. Yoshida, T. Okuzono, and K. Sakagami. Implementation of a frequency-dependent impedance boundary model into a room acoustic solver with time-domain finite element method. *Acoustical Science and Technology*, 41(6):819–822, 2020.
10. F. Ping, A. P. Engsig-Karup, C-H. Jeong, J. S. Hesthaven, M. S. Mejling, and J. Strømman-Andersen. Time domain room acoustic simulations using the spectral element method. *The Journal of the Acoustical Society of America*, 145(6):3299–3310, 2019.
11. F. Müller, D. Schötzau, and Ch. Schwab. Discontinuous galerkin methods for acoustic wave propagation in polygons. *Journal of Scientific Computing*, 77(3):1909–1935, 2018.
12. G. Sun. Symplectic partitioned Runge-Kutta methods. *Journal of Computational Mathematics*, 11(4):365–372, 1993.
13. Cs. Huszty and G. Firtha. Prediction of surface impedance impulse responses from frequency-dependent sound absorption coefficients. In *submitted to Proceedings of INTER-NOISE 2023*, Chiba, Greater Tokyo, Japan, August 2023.